# Plastic flow instability in austenitic stainless steels at room temperature: Macroscopic tests and microstructural analysis

K. Nalepka [a,*], J. Tabin [b], J. Kawałko [c], A. Brodecki [b], P. Bała [c], Z. Kowalewski [b]

[a] AGH University of Krakow, Faculty of Mechanical Engineering and Robotics, 30-059, Krakow, Poland
[b] Institute of Fundamental Technological Research, Polish Academy of Sciences, 02-106, Warsaw, Poland
[c] AGH University of Krakow, Academic Centre for Materials and Nanotechnology, 30-059, Krakow, Poland

ARTICLE INFO

ABSTRACT

AISI 304 steel experiences plastic flow instability during tension at room temperature if appropriate conditions are applied: a low strain rate and a sufficiently long gauge section of the sample. Then, propagation of the strain-localised band is activated. The electron backscattered diffraction (EBSD) research revealed that the reason is not only the difference in the content of the secondary phase – martensite α' across the front face, but also the change in the volume fraction of austenite grains with Copper (Cu) and Goss-Brass (GB) orientation. Consequently, there is a division between two areas of high and limited deformation capacity. The tendency to maintain the continuity of deformation fields induces a massive rotation of austenite grains to Cu and GB orientations, which then undergo shearing and phase transformation. As a result, momentary strain accumulation leaves behind a stiffer zone. It is shown that the trapping of austenite grains prone to large deformations, inside the matrix with Cu and GB orientations, makes the formation of a plastic strain front possible. These features improve the ductility and strength of the 304 steel over 316L and 316LN at room temperature. The in-situ EBSD tension studies for the considered grades reveal three developing textures, with their comparison showing a gradual decrease in the preferences of the Cu and GB components. Thus, the appearing bands of the accumulated strains in 316L are limited by the Cu and GB areas, while such blockages do not occur in 316LN. The presented strengthening mechanism is confirmed by the digital image correlation (DIC) measurements. The root-mean-square (RMS) function of strains along the tensile direction, characterising the linear surroundings of the considered point, is introduced as a tool for linking the micro and macro scales. The experimental results provide a basis for explaining discontinuous front propagation at a temperature near 0 K.

## 1. Introduction

Austenitic stainless steels (ASSs) of AISI 304 (EN X5CrNi18-10), AISI 316L (EN X2CrNiMo17-12-2), AISI 316LN (EN X2CrNiMoN17-11-2) grades are characterised by excellent mechanical properties and corrosion resistance in a wide temperature range (4 K - 900 K). Thus, they find numerous applications in the automotive, aviation, nuclear (Devred, 2004) and chemical industries, as well as in space and superconducting technology (Bertinelli et al., 2006; Fernández-Pisón et al., 2021), where temperature changes from room temperature to even absolute zero. It is well known that the plastic behaviour of metastable ASSs is controlled by

---

temperature (Obst and Nyilas, 1991; Pustovalov, 2008). This effect is shown by stress-strain curves obtained for the austenitic stainless steel (ASS) 316L subjected to uniaxial tension at 4 K, 77 K, and room temperature (see Fig. 1a) (Tabin, 2021). During tensile tests of austenitic stainless steels at the liquid helium temperature (4 K), the unusual behaviour of plastic flow instability can be observed. This effect, also called discontinuous plastic flow (Seeger, 1957; Skoczeń, 2008; Tabin, 2021), serrated yielding or intermittent plastic flow (Pustovalov, 2008; Schmidt et al., 2022), is reflected by stress oscillations on the stress-strain curve. Thermal and kinematic characterisation of plastic flow instability in 316L at 4 K is presented by Tabin et al. (2016) and Tabin (2021). In general, intermittent plastic flow instability occurs below the $T_1$ temperature due to a change in the deformation mechanism in which edge dislocations dominate instead of screw ones (Obst and Nyilas, 1991). The $T_1$ temperature is strongly dependent on the chemical composition and strain rate, and for the metastable 304 or 316L ASSs it is about 35 K (Pustovalov, 2008). Above the $T_1$ temperature, the intermittent plastic flow instability is eliminated, but under special conditions, a Lüders-type deformation can be observed (Fig. 1b). A characteristic feature of the phenomenon is a band of localised plastic strains, stably propagating along the tension direction (Gao et al., 2019). It turns out that such behaviour occurs at room temperature for a 304 steel specimen with a gauge length that is long enough and below the critical strain rate (Fig. 1b) (Tabin et al., 2023). Therefore, the different modes of plastic flow instability in the ASSs are observed depending on the temperature.

As the temperature decreases to absolute zero, metastable ASSs exhibit an increasing tendency towards diffusion-free phase transformation during plastic deformation (Angel, 1954; Olson and Cohen, 1975; Spencer et al., 2009). In this process, initial austenite with a face-centred cubic (FCC, γ) structure transforms into martensite ε with a hexagonal close-packed (HCP) structure and subsequently into martensite α' with a body-centred cubic (BCC) structure. It is worth noting that the transformation can also occur directly, i.e. γ→α', and mainly martensite α' is observed during tension at room temperature. (Spencer et al., 2009; Nalepka et al., 2021). Experiments prove that the strain-induced phase transformation in ASSs at the liquid helium temperature is coupled with intermittent plastic flow (Tabin et al., 2019; Tabin, 2021; Schmidt et al., 2022; Nalepka et al., 2024). It is worth pointing out that, for combined stresses, it is unclear whether the transformation is stress-induced or strain-induced (Das et al., 2011). Therefore, in our study, the term "deformation-induced phase transformation" is used (Das et al., 2011).

The schematic illustration of coupling between the phase transition and the intermittent plastic flow is presented in Fig. 1a. After reaching the yield point, the first serration occurs, indicated by an abrupt drop in stress. The macroscopic shear band fully develops and penetrates across the specimen gauge length, significantly increasing the volume fraction of the secondary phase in the sample (Tabin, J., 2021). This takes place until the macroscopic shear band reaches one of the specimen's shoulders (Lüders-type strain). Then, the shear band starts to propagate randomly. This stage takes place until a rupture of the specimen occurs. Further experimental evidence for the coupling of intermittent plastic flow of ASSs and the phase transformation is provided by Schmidt et al. (2022). The authors determined the amount of martensite α' per serration and the propagation rate of the phase transformation front consisting of the subsequent shear bands. Thus, the strongly localised deformation induces intensive phase transformation, which consequently blocks the shear band and switches it to another place. As a result, martensite α' generates the so-called delocalisation effect, which leads to the multiple necking pattern commonly observed after the uniaxial tension of metastable ASSs at cryogenic temperature. In-depth insight into the shear band structure and the coupling of intermittent plastic flow with the phase transformation in the 316L steel subjected to tension at 4 K is provided by Nalepka et al., 2024. The synchrotron research revealed an uneven distribution of martensite α' in the narrowing zone formed after the first serration. The volume fraction of the secondary phase is greatest at the boundary of the shear band, efficiently blocking its propagation. The value is three times higher than that in the strain localisation place. The obtained result shows that shear stress may be of greater importance for the phase transformation than strain concentration. To efficiently
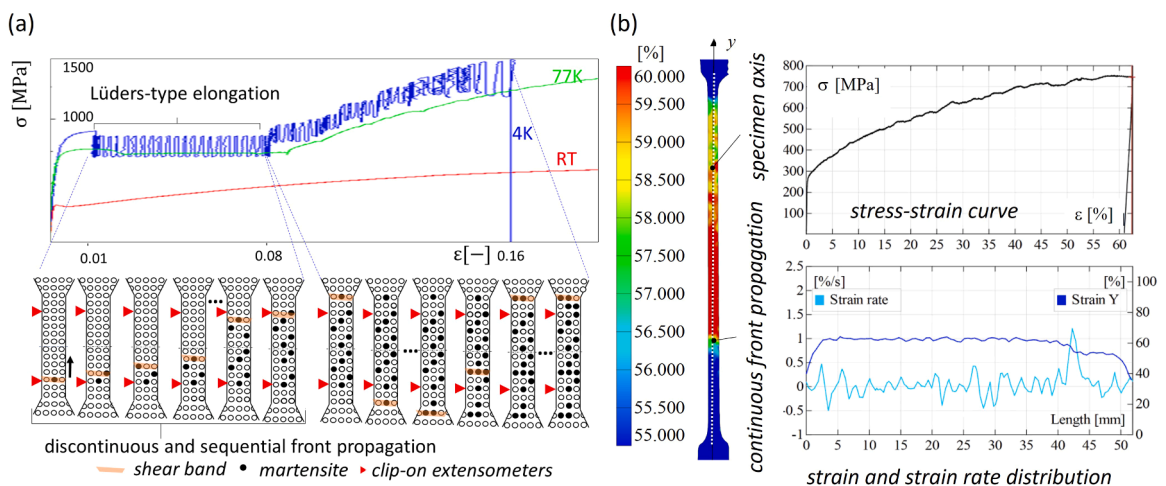


**Fig. 1.** Plastic flow instability in austenitic stainless steels in a wide range of temperatures. (a) Uniaxial tensile tests of 316L at 4 K, 77 K, and room temperature: engineering stress (σ) - engineering strain (ε). Schematic illustration of strain localisation and front propagation during tensile tests of austenitic stainless steel (316L) at 4 K (Tabin, 2021). (b) Uniaxial tensile test of 304 at room temperature: engineering stress (σ) - engineering strain (ε) curve, strain ($ε_y$) and strain rate ($dε_y/dt$) distribution along the y axis (Tabin et al., 2023).

predict martensite development a general thermodynamic approach based on the modified transformation work, proposed by Levitas et al. (2017), seems to be most appropriate.

Many authors have investigated the phase transformation and its coupling with the mechanical properties of the 300-series stainless steels under combined loadings and in a wide range of temperatures. Nevertheless, full-coupled structural and microstructural analyses in a wide range of temperatures have not yet been carried out. Spencer et al. (2009) showed that an intensive martensitic transformation in 316L leads to a Lüders band propagation along the tension direction. The effect observed at 77 K was induced by pre-strain at room temperature. In this way, a dislocation structure was created, providing potential nucleation sites of α'. Lüders-type deformation in 304L and 316L at 77 K was also observed by Li et al. (2020). The authors identified that the captured shear band consists of 80 % martensite, while regions far away from the shear band are composed mainly of austenite. A comprehensive study on the strain-induced martensitic transformation in the 304 stainless steel is presented by Cios et al. (2017). The authors used a number of complementary techniques, such as dilatometry, calorimetry, magnetometry, and in-situ X-ray diffraction coupled with high-resolution microstructural transmission Kikuchi diffraction analysis. The test parameters for the effective TRIP (transformation-induced plasticity) effect were identified in light of the conducted study. From the macroscopic perspective, the influence of deformation temperature on the strain hardening of the 304 steel was presented. In this context, the maximum reaction rate of $\gamma \rightarrow \alpha'$ transformation was found to have a linear correlation with temperature. Extensive EBSD studies have revealed a heterogeneous distribution of the secondary phase in the $\gamma$ matrix. Martensite embedding is strongly related to the austenite texture. Nalepka et al. (2021) investigated an evolution of the 316L microstructure in symmetrically notched specimens at 4 K. As a narrowed section is approached, a uniaxial stress state is replaced by a complex one with significant stress components. In consequence, the austenite grains rotate more intensively, striving for the preferred Brass (B) orientation. Applying X-ray diffraction with the use of synchrotron radiation revealed a certain asymmetry of the process. An orientation close to only one of the two B variants is formed with a high frequency. EBSD studies show that the rotation of grains to the final, stable position is blocked by martensite generated at the intersection of slip bands. Another way to achieve the B orientation is by forming twin boundaries. They are arranged in bands, which become barriers, piling up dislocations since they run through many grains. Breaking them leads to intermittent plastic flow, during which martensite α' is generated. The relationship of austenite texture with the deformation mechanisms of the 304 steel at room temperature was studied by Polatidis et al. (2019). The different orientation of the grains $\gamma$ was obtained by applying two loading paths: uniaxial and equibiaxial tension. During the first test, the evolving crystallographic texture favoured deformation twinning and delayed the deformation-induced martensitic transformation. On the other hand, during equibiaxial loading, the strain was accommodated by slips along multiple slip planes, which provided nucleation sites for the martensitic transformation. Thus, the deformation mechanisms are strongly influenced by the austenite texture, which is controlled by the loading path. In contrast to 304 and 316L, the 316LN ASS has a strongly reduced ability to undergo the phase transformation. Thus, it is used as a non-magnetic jacket for low-temperature superconductors, working even at 4 K. Nitrogen is an efficient stabiliser of austenite, which makes twinning the primary deformation mechanism. In-situ transmission electron microscope (TEM) analysis by Han et al. (2018) reveals the intensive formation of twins before the ferromagnetic martensite α' during loading at 77 K and 4 K. Furthermore, nitrogen improves mechanical properties by solid-solution strengthening and precipitation strengthening.

This work aims to investigate the plastic flow and hardening processes of the metastable 304 and 316L steels in the context of 316LN, which is stable against martensitic transformation. The basis constitutes tensile tests at room temperature recorded in-situ with the use of two techniques: DIC and EBSD. In this way, the development of deformation fields and the accompanying evolution of the microstructure are identified. The coupling of these observations allows the mechanism of unstable plastic flow to be explained.

## 2. Materials and experiments

Uniaxial tensile tests were carried out for ASS 304, 316L, and 316LN at room temperature with the use of two in-situ techniques, DIC and EBSD, to identify the strain processes characteristic of the individual steel grades and the underlying microstructure evolutions. The traverse rate was assumed to be 1.0 mm/min ($\dot{\varepsilon} = 5.5 \cdot 10^{-4}$ s$^{-1}$) to trigger the unstable plastic flow in the 304 ASS, according to the research by Tabin et al., 2023. Activating this effect also requires the appropriate gauge length, which was applied to the dog-bone specimens in DIC experiments (Fig. 2a). The EBSD tests were performed using samples with a different geometry (Fig. 2b) due to limitations that are imposed on the technique. The uniaxial tension of such specimens, with a short gauge length, leads to the localisation of the complex strain state, which eliminates the propagation of plastic instability (Tabin et al., 2023). Thus,
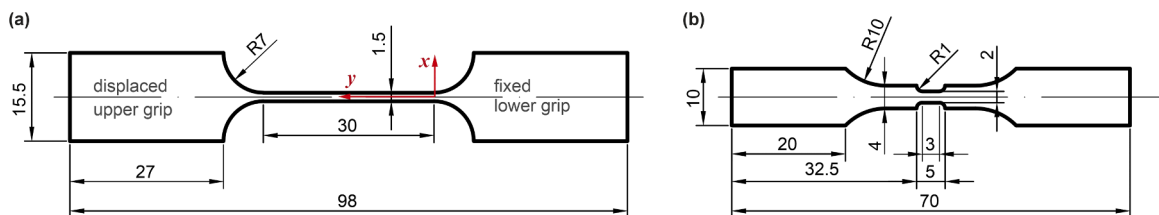


**Fig. 2.** The geometries of specimens used in the tensile tests. (a) A dog-bone specimen applied in DIC measurements, with the $y$ axis running along the symmetry axis of the sample from the bottom limit of the gauge region towards the upper grip displaced in a test machine. (b) A specimen applied in EBSD investigations. Dimensions are in mm; the specimens' thickness is 2 mm.

microstructural evolutions without the presence of the strain front were registered and collated with the EBSD images of the areas before and after the strain front, induced and arrested in the dog-bone samples during the DIC experiments. Such an approach allows the sequence of microstructure changes that leads to the unstable flow to be uncovered, improving the ductility of the 304 ASS in comparison to 316L and 316LN.

The chemical compositions of materials are presented in Table 1. It is worth noting that interstitial elements, C and N, increase the yield and ultimate strength of ASSs. Nitrogen is particularly efficient since it promotes planar slips, stacking fault formation, and twinning (Wang et al., 2023). Its beneficial influence on mechanical properties significantly increases under cryogenic conditions. The substitutional elements of Si, Mn, Ni, Cr, and Mo mainly stabilise austenite. Si, Mo, and Cr contribute to an increase in the yield and ultimate strength, but to a lesser extent than N (Naghizadeh and Mirzadeh, 2018). Ni, like Cr and Mo, improves corrosion resistance but also enhances ductility. The addition of Ni causes grain coarsening, a reduction in dislocation density, and twin-induced softening, which leads to a decrease in the tensile strength (Zhang et al., 2024).

One of the key quantities conditioning the mechanical response of a material is the stacking fault energy (SFE). According to the formula proposed by Meric de Bellefon et al. (2017) and recognised by Janeiro et al. (2022) as very useful, SFEs for the studied 304, 316L, and 316LN ASSs at room temperature are as follows: 17.1, 23.3, and 26.3 mJ/m$^2$. The phase transformation is promoted if SFE is less than 18 mJ/m$^2$; twinning is preferred at the intermediate values of 18 – 45 mJ/m$^2$; while higher SFE makes dislocation glide the main mechanism of plastic deformation. The values determined for the considered steels show that twinning contributes significantly to their deformation processes. Moreover, the 304 ASS tends to undergo martensitic transformation.

The specimens were fabricated using electrical discharge machining (EDM) from a commercial stainless steel sheet (304, 316L) and bar (316LN) with the tensile axis parallel to the rolling direction (RD). The materials were supplied in the annealed (316LN) and in cold-rolled and annealed conditions (304 and 316L, according to the ASTM A480 and EN 10088 standards). In such a form, the materials are typically used for structural components working in cryogenic conditions, down to the temperature of superfluid helium, 1.9 K (Bertinelli et al., 2006). The initial microstructure (Fig. 3) of the as-received materials in all cases consists of equiaxial, fully recrystallised grains with recrystallisation twins present in some of the larger grains. The average grain size is comparable in the 304 and 316L steels, equalling 15.6 μm and 19.2 μm, respectively, while 316LN has a coarse microstructure with an average grain diameter of 158.8 μm. All three steels have a heterogeneous distribution of grain sizes. During the deformation, grains with large diameter discrepancy can behave differently. Fine grains are harder to deform with dislocation glide, and twinning in fine grains is generally suppressed. However, in the investigated steels, the fine grains are homogeneously distributed in the microstructure, and most importantly, they constitute only a small fraction of the overall microstructure. In the case of the 304 steel, fine grains (grains with a diameter below 0.33 of the average diameter) constitute only 5.7 % of the observed area, while grains with a diameter above the average constitute 40.8 % of the area. For 316L, the grain fraction constitutes 5.3 % and 46.7 % of the observed area, respectively. For 316LN, the values are 6.3 % and 45.8 %, respectively. Due to the relatively low fraction of fine grains and their homogeneous distribution, it is considered that the initial grain size distribution has a low impact on the macroscopic deformation behaviour and strain delocalisation in the investigated steels. A reduction in austenite grain size generates a more stable structure against the phase transformation. This effect is shown by a commonly used quantity - the temperature $M_{d30}$ at which a 30 % true strain induces a 50 % volume fraction of martensite α' (Nohara et al., 1977; Rocha and Oliveira, 2009). Therefore, to provoke higher instability, 316LN has a coarse microstructure with a significantly larger average grain diameter than either of the 304 or 316L steels. As a result, the temperature $M_{d30}$ for 304, 316L, and 316LN amounts to -0.54, -126.48, and -250.13 °C, respectively.

The DIC and in-situ EBSD techniques are used during displacement-controlled tensile tests to analyse the structural behaviour of the specimen and the deformation mechanism of austenitic stainless steels.

DIC is a vision-based data acquisition technique in which two CCD cameras, light sources and a data acquisition system (DAQ) are integrated. In this method, the specimen needs to be covered with a special black-and-white pattern. Based on the pattern, the co-ordinates of the specimen are defined. The origins of the rectangular-shaped pattern are directly applied to calculate the displacement and strain (Kopec et al., 2021). The strain distribution during tension is monitored by a DIC Aramis 12 M equipped with lenses of a total focal length of 75 mm and calibration settings appropriate to the measuring area equal to 170 × 156 mm or 38 × 25 mm. The calibration is performed before testing using a certified GOM calibration plate.

The in-situ EBSD investigations were performed in an FEI Versa 3d FEG scanning electron microscope (SEM) with the use of a Kammrath & Weiss (K&W) tensile-compression stage, equipped with a 5 kN load cell and a linear optical transducer for displacement control. During the in-situ experiments, the tensile stage with the EBSD-shaped specimen (Fig. 2 b) was placed inside the SEM. For the in-situ imaging, the K&W stage was installed in the pre-tilted configuration, allowing the EBSD analyses to be performed without unloading the specimen. For each of the EBSD investigations, the actual strain of the specimen was determined by measuring the displacement of the specified features on the specimen surface, such as triple junctions of characteristic grains. For each specimen, EBSD maps were collected for the strains 0 %, 20 % and 50 %, corresponding to strain levels calculated from the analysis of

**Table 1**
Chemical composition of the tested steel grades.

| | Chemical composition wt.% | | | | | | | | |
|---|---|---|---|---|---|---|---|---|---|
| | C | Si | Mn | Ni | P | S | Cr | Mo | N |
| 304 | 0.070 | 0.25 | 1.9 | 8.27 | 0.05 | 0.02 | 18.7 | 0.22 | 0 |
| 316L | ≤0.030 | 0.30 | 1.98 | 11.05 | 0.02 | 0.096 | 17.85 | 2.09 | 0.1 |
| 316LN | 0.029 | 0.39 | 2.04 | 12.62 | 0.012 | 0.003 | 19.12 | 2.99 | 0.2 |
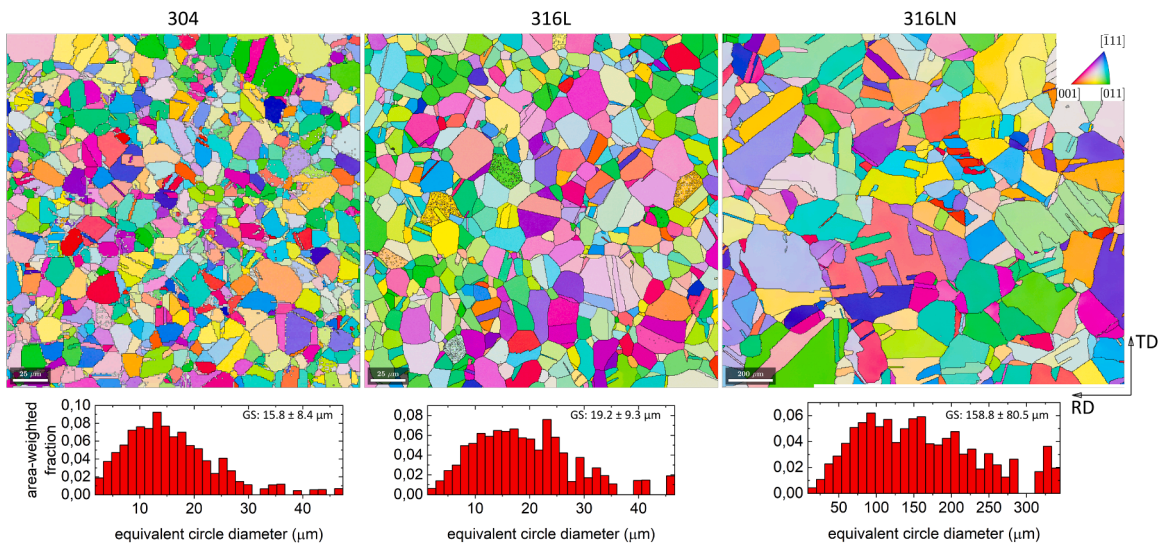
**Fig. 3.** As-received microstructures of the investigated materials: inverse pole figure (IPF) maps in the top row and grain size distributions (equivalent circle diameter) in the bottom row. Notice the different scale of the 316LN IPF map (on the right). IPF colouring is performed relative to the normal direction (ND), perpendicular to the surface specimen. The images are taken in a coordinate system formed by the rolling direction (RD) parallel to the tension direction and transverse direction (TD).

microstructure features displacement. This is 0 %, 12.2 %, and 28.6 % for 316L, 0 %, 11.4 %, and 27.9 % for 304, and 0 %, 14.3 %, and 27.0 % for 316LN.

Additionally, ex-situ experiments were carried out to confirm tendencies to form different textures underlying dissimilar deformation fields registered by the DIC method in the studied steel grades. During this research, the specimen was subjected to uniaxial tension to predetermined strain levels, upon which the specimen was unloaded, removed from the tensile stage, and placed inside the SEM for EBSD analysis. Subsequently, the specimen could be re-installed at this stage, and the tension was continued. Moreover, the EBSD investigation of pre-strained specimens during uniaxial tensile tests was also performed. The strain to which the specimen was deformed for each EBSD measurement step was determined based on the displacement of the tensile stage frame using the optical transducer.

The EBSD maps were collected using the Oxford Aztec system with a Symmetry S2 CMOS EBSD detector. Data was acquired using an accelerating voltage of 20 keV and beam current of 48 nA in the "Speed 2" mode of the Symmetry S2 detector using a pattern resolution of $156 \times 128$ px. The detector exposure was adjusted depending on the deformation state of the specimen, typically resulting in ~1450 pps for non-deformed specimens with good pattern quality and ~600 pps for deformed specimens with deteriorated pattern quality. The registered patterns were background corrected, and typical Hough-based indexing was performed with up to 12 Kikuchi bands detected. Three crystal symmetries were considered for the phase identification: cubic Fe-FCC, space group 225 ($a=b=c=3.6599\ Å$), cubic Fe-BCC, space group 229 ($a=b=c=2.8660\ Å$), and hexagonal Fe space group 194 ($a=b=2.4730\ Å$, $c=3.9620\ Å$). The EBSD measurement grid (map size and spatial resolution) was chosen for each material depending on the initial grain size to ensure an adequate number of grains for texture analysis: 400 mm x 250 mm with a 0.35 step size for 304 specimens; 150 mm x 120 mm with a 0.2 step size for 316L specimens, and up to 6700 mm x 2660 mm with a 3.5 mm step size for 316LN.

For the SEM-EBSD analysis, the surface of specimens was prepared by a combination of mechanical grinding/polishing methods (SiC papers grit up to #2000, followed by diamond suspension polishing with grain sizes of 3 mm, 1 mm, and final polishing with 60 nm colloidal aluminium oxide suspension), and electrolytic polishing using electrolyte consisting of 10 % perchloric acid and 90 % acetic acid. The electrolytic polishing constant voltage of 25 V was applied between the specimen and cathode, the electrolyte was kept at room temperature, and the electropolishing time was adjusted to obtain a shiny surface finish.

## 3. Plastic flow instability at room temperature

The displacement-controlled uniaxial tensile tests of dog-bone specimens of the 304, 316L and 316LN ASSs are carried out at room temperature. The 3D strain distributions for different traverse displacements ($\Delta l$ mm) are presented in Fig. 4. Moreover, it presents the engineering stress-engineering strain curves (black curve) and strain amplitude along the specimen axis ($\varepsilon_y$ %, blue curve).

In the initial stage of deformation ($\Delta l$=0.5 mm, Fig. 4b), the uniform strain distribution is observed for the 304 and 316L steels, while for 316LN, strain localisation already occurs. The strain amplitude (peak to peak) at $\Delta l$=7 mm of traverse displacement becomes significantly higher for 316LN. Necking is observed in the 316LN steel for further tension, and then a fracture appears ($\Delta l$=14 mm, Fig. 4c). It is worth pointing out that the test machine's traverse pulls the specimen's upper grip during the test. Therefore, a slight drop in strain distribution in 304 and 316L is observed as a result of the minor misalignment. For $\Delta l$=18 mm in the 316L steel, a neck formation is observed. Then, the plastic strain develops in the neck until a rupture occurs. At the same time, strain delocalisation is
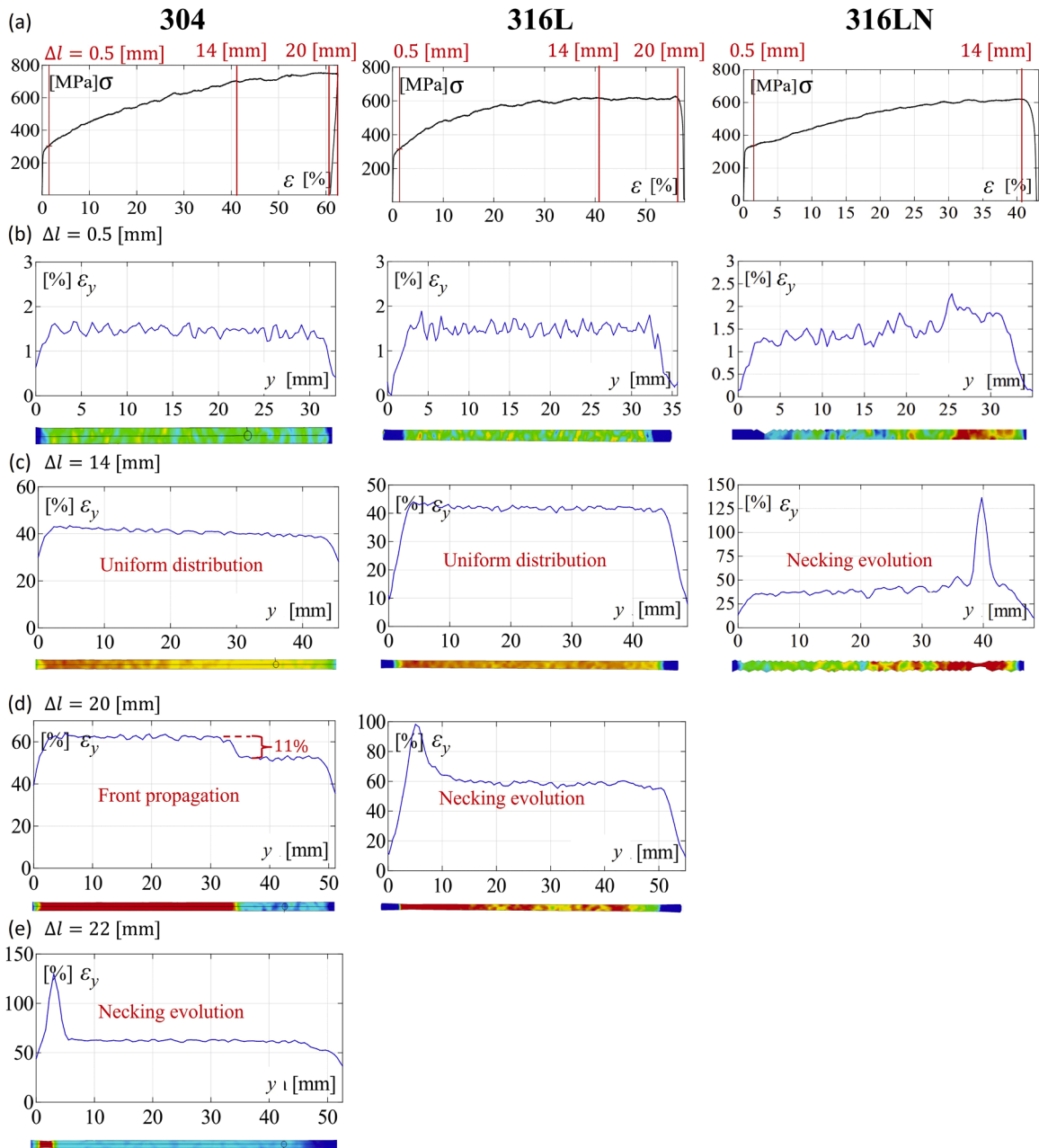
**Fig. 4.** Kinematically-controlled uniaxial tensile tests of 304, 316L, and 316LN at room temperature. (a) Engineering stress ($\sigma$) - engineering strain ($\varepsilon$) curves. The strain amplitudes ($\varepsilon_y$) along the axes of samples as functions of distance ($y$) from the bottom limit of the gauge section, as well as strain distributions in the gauge region obtained for different traverse displacements $\Delta l$: 0.5 mm (b), 14 mm (c), 20 mm (d), 22 mm (e).

observed for the 304 steel, and the propagation of the plastic strain front across the specimen arises (Fig. 4d).

Front propagation is distinguished by a significant strain increase, even exceeding 10 % (Fig. 4d). When the front overcomes the specimen's gauge length, a neck formation is observed, and a fracture occurs. It should be emphasised that the front propagation at room temperature is observed only in the metastable 304 steel. For this steel grade, a tendency towards deformation-induced phase transformation is higher compared to 316L or 316LN. Nevertheless, uniform deformation is observed before the stable propagation of the strain-localised band occurs in the 304 steel (Fig. 4c).

The following question arises: is it possible to distinguish quantitatively and qualitatively the differences in macroscopic strain distribution between the 304 and 316L steels in the initial uniform stage? Until a front formation or necking occurs, limited fluctuations of strain distribution are observed in the specimen gauge area of the 304 and 316L steels (Figs. 4c and 5a). It is worth pointing out that the distribution of local strain maxima during loading maintains its spatial orientation (Fig. 5a). To precisely examine the

homogeneity of strain field distribution in the 304 and 316L steels, the floating root mean square (RMS) function of strain amplitude along the symmetry axis is evaluated (Fig. 5b) (Tabin and Brodecki, 2024).

Generally, the RMS values are always positive and measure the energy of a signal, in this case, the strain amplitude along the symmetry axis. It replaces each strain value $\varepsilon_y$ along the specimen axis (Fig. 2a) by the RMS value ($\varepsilon_{RMS}$) calculated from the actual value and a specified number of neighbouring values. The exact number of adjacent values on the bottom and upper sides is used to maintain the symmetry of the problem. Considering the point on the specimen axis $j$, an odd $N$-element data set is obtained. The considered values are determined by the radius $R = \frac{N-1}{2}$. So, for $R = 10$ the RMS is calculated by a moving window with the central value $\varepsilon_j$ and 10 values on each side, which gives 21 values. One can note that point $j$ is not duplicated by the symmetry. Thus, its contribution is reduced by a weight of 0.5. Using the same weight for the last point, the RMS function (the one-side function) is obtained in the following form:

$$\varepsilon_{RMS} = \sqrt{\frac{1}{N-1}\left(0.5 \cdot \varepsilon_j^2 + \varepsilon_{j+1}^2 + \varepsilon_{j+2}^2 + \ldots + \varepsilon_{j+N-2}^2 + 0.5 \cdot \varepsilon_{j+N-1}^2\right)} \qquad (1)$$

If there are fewer values at the boundaries, the calculation runs with fewer values at one end. The RMS function of strain along the symmetry axis is calculated for different strain levels ($\varepsilon_{ext} = 2\%, 10\%, 30\%, 50\%, 55\%$), measured by means of extensometers (gauge length equal to 25 mm). The results are presented in Fig. 5b. Below $\varepsilon_{ext} = 10\%$, the RMS of strain amplitude is similar for both steel grades. As the specimen's total elongation increases, the strain's RMS for 316L becomes higher than that for 304. Above $\varepsilon_{ext} = 50\%$, the RMS function is strongly inhomogeneous for 316L. The RMS of strain along the sample symmetry axis indicates a strain accumulation, which is far greater for 316L than for 304, in particular above $\varepsilon_{ext} = 30\%$. The presented RMS function appears to be an efficient tool for detecting the heterogeneity of strain distribution along the specimen. The more accurate analysis obtained in this way is a step towards microstructural investigations. Thus, the RMS function enables the linking of the results registered at the macroscopic level with the observations performed at the microscopic scale. This issue will be continued in the next section.

The plastic strain front propagation in 304 specimens is observed as a kind of unstable plastic flow during tension. It is observed at room temperature regardless of specimen width (Fig. 6). Nucleation of the plastic front occurs at different locations, predominantly near the upper gauge limit (Fig. 6, for widths of 1 and 3 mm). However, in a 2 mm wide specimen, this phenomenon arises halfway along its length. One of the reasons for this observed pattern is the non-proportionality of the tested specimens, as classified in the ISO 6892-1:2019 standard. Consequently, the critical area is frequently located near the upper adjustable grip. However, the specimens maintain the geometry required for tensile tests at 4 K due to space constraints and the need to balance the stiffness ratio between the cryostat and the specimen (Nalepka et al., 2024). This consistency allows for a reliable comparison of plastic flow instability in the temperature range from 4 K to 300 K.

The impact of the other test parameters, including strain rate and gauge length limits, has been identified previously (Tabin et al., 2023). That investigation was based on in-situ tensile tests conducted at room temperature and recorded using DIC. The current work discusses the DIC results in a much broader context of the in-depth microstructural and texture analysis.

## 4. Microstructure

Initially, the austenitic texture of the 316L steel contains a dominant component close to the brass orientation, belonging to the two fibres α and β. The volume fraction of each of them in the orientation space amounts to 24 % and 16 %, respectively. Due to the presence of the β fibre, besides the orientation of the brass (B), two additional ones are formed: S and Cu (Fig. 7a). The B orientation occurs 2.6 times more often than the random one (rdm), while the others are characterised by a frequency of 2.2. The α fibre introduces subsequent texture components with a small content at the initial state: Goss (2.2 rdm) and Goss-Brass (1.6 rdm).

The tension in the rolling direction (RD) enhances the initially present fibres α and β (Fig. 7b). When the longitudinal strain reaches 12 %, the volume fraction of the first and second one increases to 26 % and 18 %, respectively. The main reason for the stronger, fibrous texture is the increased preference for the specific orientations of Cu, B, Goss-Brass (GB), S and Goss (G). The heterogeneous distribution of the orientation function along the fibres α and β indicates the dominance of the first two components (Fig. 7b).
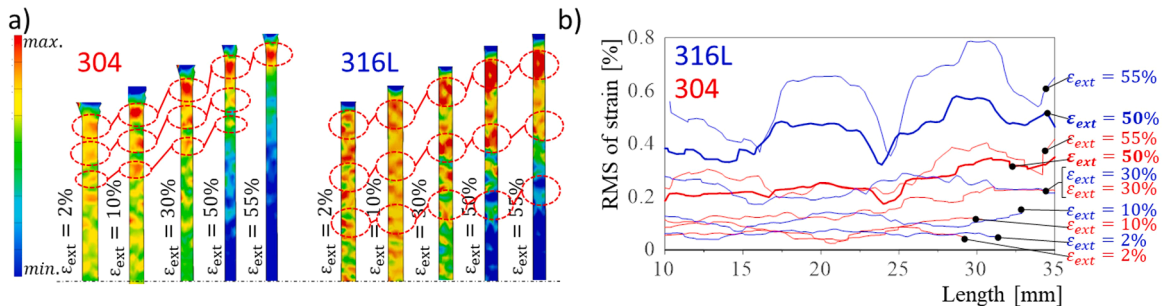


**Fig. 5.** Uniaxial tensile tests of the 304 and 316L steels at room temperature; a) the maximum strain $\varepsilon_y$ distribution during loading maintains its spatial orientation; b) RMS of strain amplitude for the 304 and 316L steels. The RMS values are defined for different strain levels $\varepsilon_{ext}$ measured by extensometers (Tabin and Brodecki, 2024).
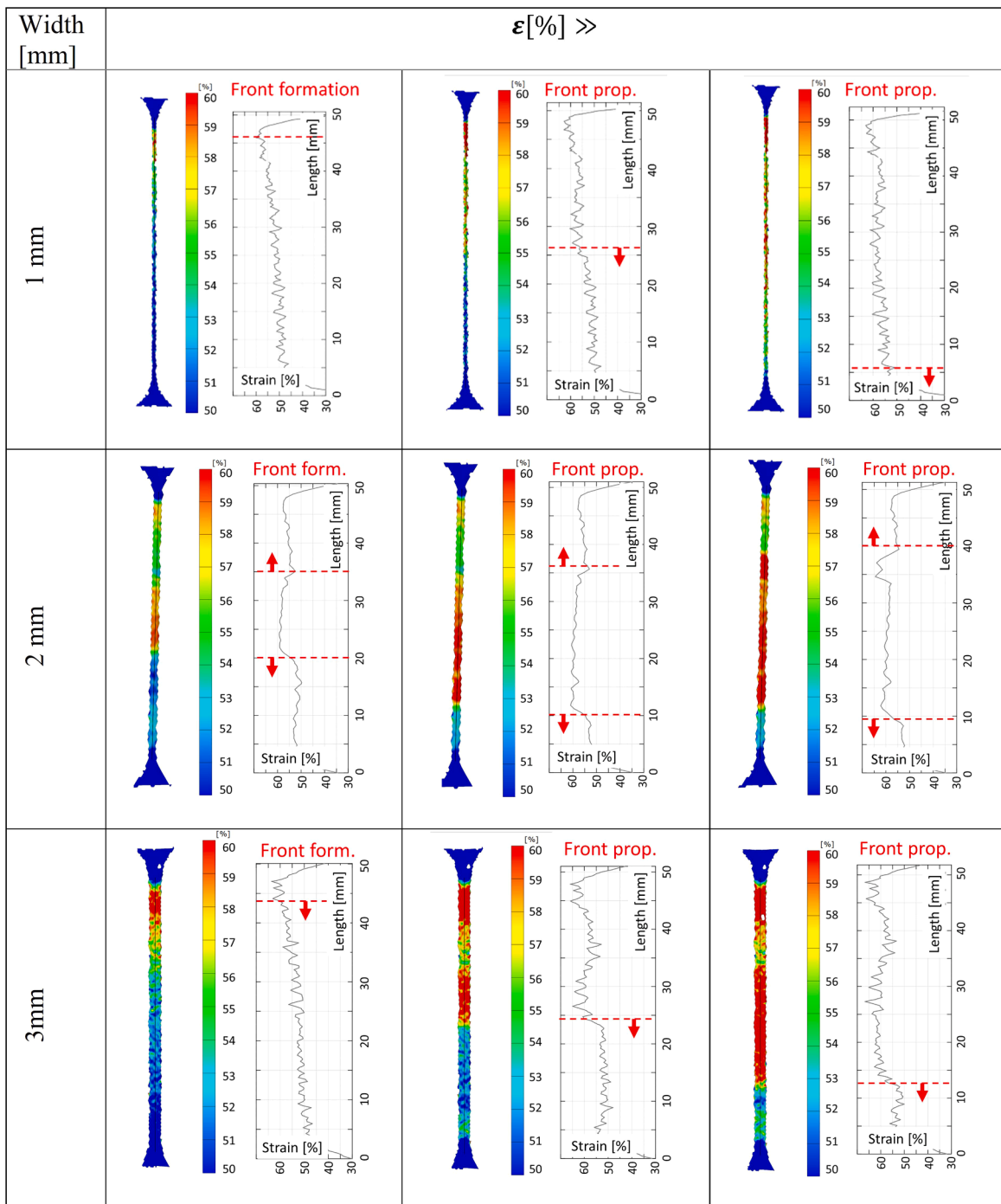
**Fig. 6.** Different modes of the front propagation in the metastable 304 stainless steel for different specimen widths (1mm, 2 mm, 3 mm) during a displacement-controlled tensile test at room temperature.

Further tension increases the frequency of occurrence for the two orientations Cu and GB. At 29 % strain, they become the dominant texture components (Fig. 7c). The B and S orientations are less pronounced, maintaining the frequency achieved at 12 % strain, while the G orientation undergoes reduction. As a result, the volume fractions of the α and β fibres increase, however more slowly, this time by 1 %. The dominance of the Cu and GB components makes the planes $\{1\,1\,1\}_\gamma$ oriented perpendicular to the tension direction four times more than the random ones (Fig. 8c), which is a result of the consistent texture evolution (Fig. 8a-c). The grains with such an orientation undergo intensive twinning, as the resolved shear stress in $\langle 1\,1\,\overline{2}\rangle\{1\,1\,1\}_\gamma$ exceeds that which arises in the slip
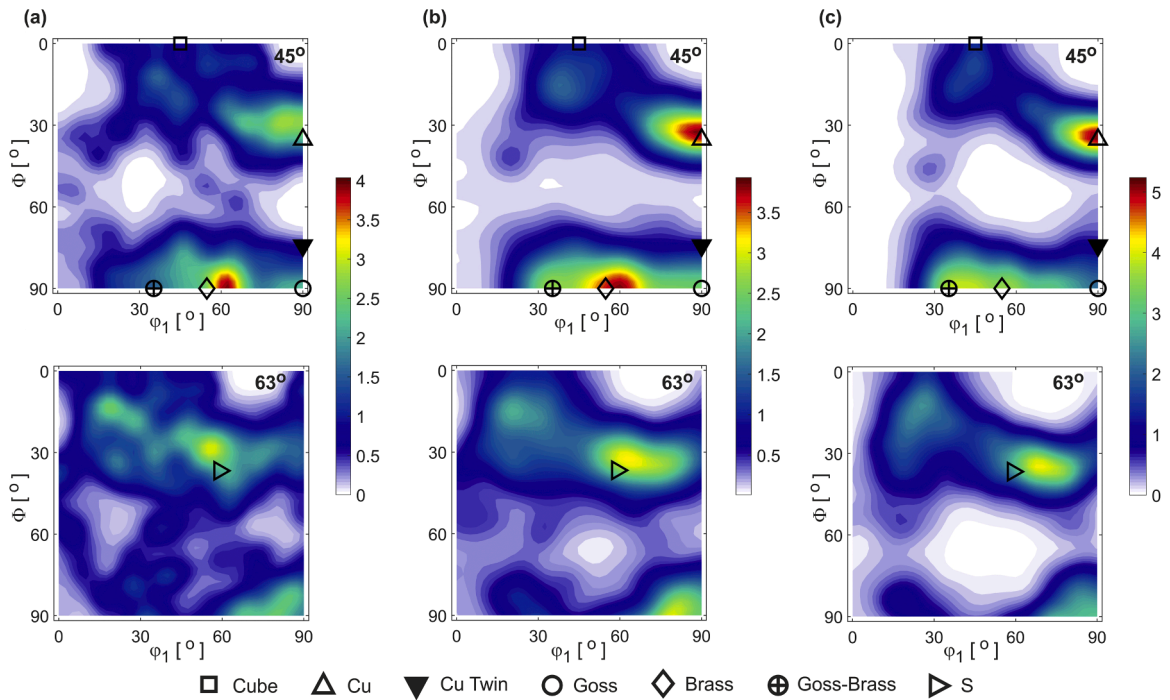
**Fig. 7.** Evolution of the austenitic texture during tension of the 316L steel. Orientation distribution function (ODF) in the Euler space for the sections $\varphi_2 = 45°$ and $\varphi_2 = 63°$ at the strain of 0 (a), 0.12 (b), 0.29 (c).

system $\langle 1\ \bar{1}\ 0 \rangle \{1\ 1\ 1\}_\gamma$. Deformation twins constitute thin plates with a thickness of several micrometres. They inhibit activation of the conjugate slip system in the matrix, consequently promoting planar glide. Thus, grains with planes $\{1\ 1\ 1\}_\gamma$ perpendicular to the tension direction have a limited ability to undergo plastic deformation. EBSD studies show that they separate narrow areas of the macro-slip bands (Fig. 9). They are located in one of the areas of strain concentration captured by the DIC method (Fig. 5a, b). Thus, EBSD investigations reveal the mechanism of the unstable flow of 316L, which is concentrated in separated bands identified both at macro and micro levels after exceeding 60 % of the relative elongation of the gauge length.

Martensite α' nucleates at the intersections of the shear micro-bands, regardless of their nature (Fig. 10). The transformation is induced by crossing martensite ε plates and twin lamellae. As a result, martensite α' is formed mainly in grains with the Cu and GB orientations prone to shearing, while those with the G orientation are only subject to strong plastic deformation (Fig. 10a, c). In particular, an intense phase transformation occurs in the shear areas in contact with the macro-slip bands. Thus, the development of these bands is blocked, and plastic strains are transferred to another area of the specimen, which leads to the dispersion of deformation concentration zones. Martensite α' begins its growth in grains with a specific orientation, embedding in a non-random manner. At the inter-phase boundaries, there is a preferred ring of misorientations determined by the orientation relations typically observed in steels Pitsch's, Kurdjumov-Sachs' (KS), and Nishiyama-Wasserman's (NW) (Fig. 10b). The fluent transition between the different orientation relations is enabled due to the room temperature at which the tension is conducted. If the loading is applied at 4 K, the Pitsch misorientation is mainly formed because it is most energetically favourable (Zwolińska-Faryj W. et al., 2022; Nalepka et al., 2023).

The initial texture of the 304 steel is significantly different than that of 316L. Instead of the α and β fibres, τ fibre is generated,
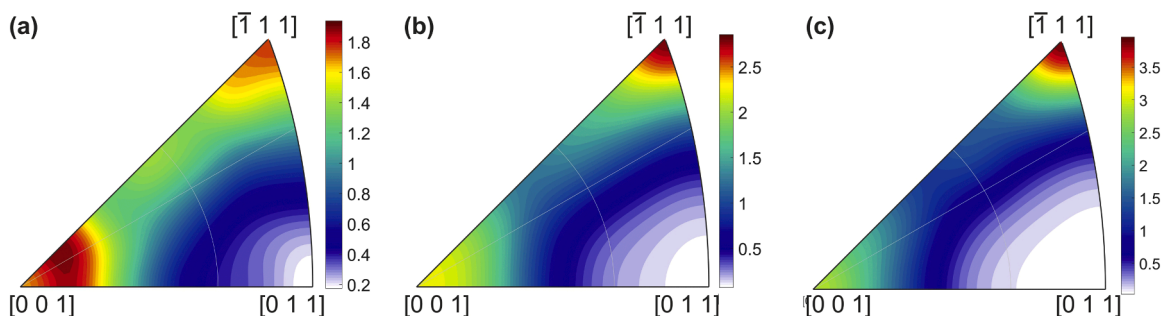


**Fig. 8.** Orientation of austenite grains of the 316L steel with respect to the tension direction at the strain of 0 (a), 0.12 (b), and 0.29 (c).
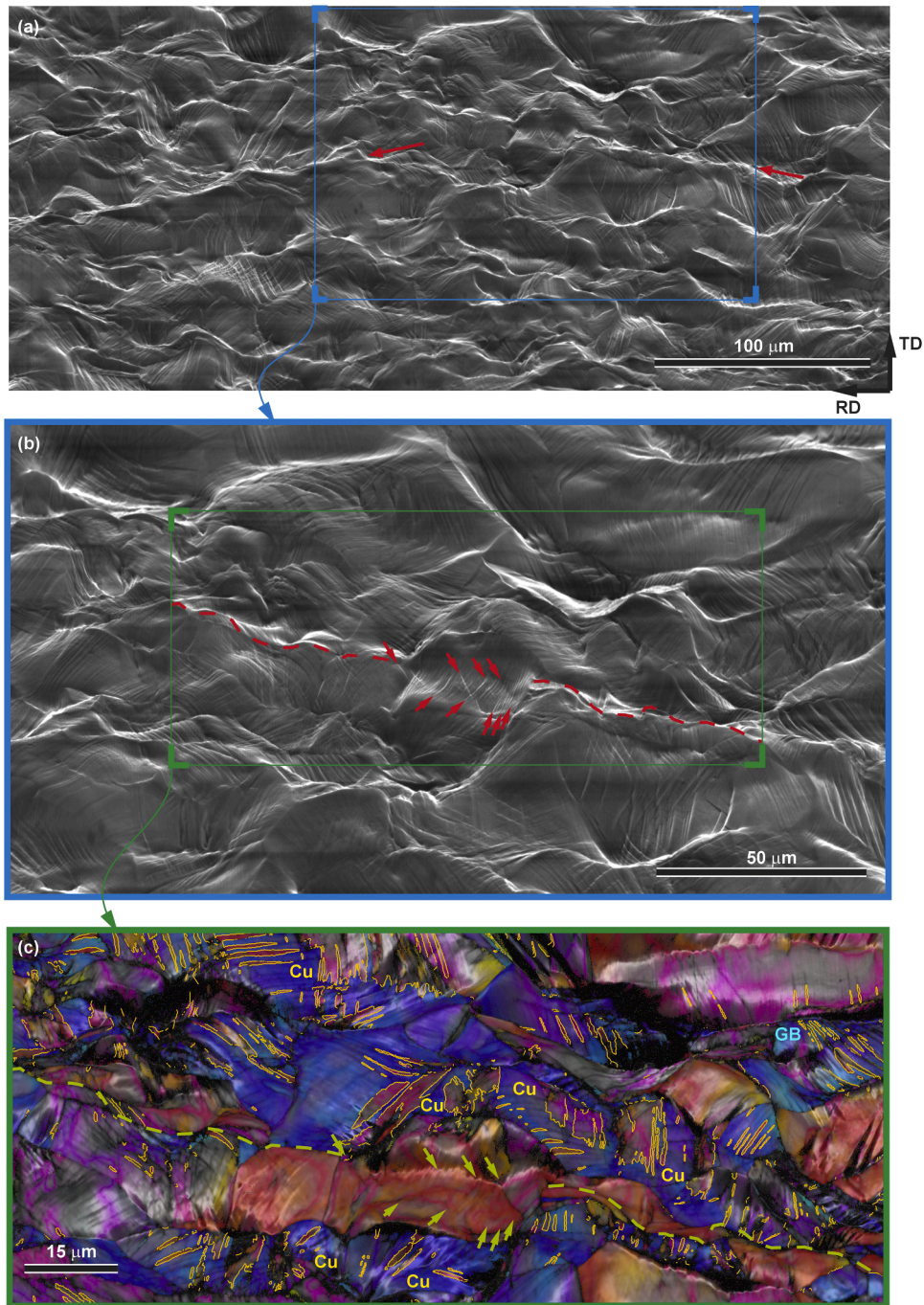
**Fig. 9.** Microstructure of a region at the centre of the 316L steel specimen subjected to the tension up to the engineering strain of 0.6. (a) SEM image of macro-slip bands with a distinguished fragment for further studies. (b) SEM image of the representative slip band marked with dashed lines, with a fragment separated for EBSD analysis. Arrows indicate traces of the active slip planes generating intensive plastic strain. (c) The representative band region in the form of an IPF map for the tensile direction superimposed on the image quality (IQ) contrast. Twin boundaries are denoted by solid yellow lines.

containing the Cu twin orientation with a high frequency of 2.7 rdm (Fig. 11a). The tension along RD leads to a strong preference for the Cu orientation, which at a strain of 11 % reaches a frequency of 3.7 rdm (Fig. 11b). As a result, the originally formed τ fibre is strengthened. At the same time, another high-preference texture component is created - GB orientation (3.2 rdm). Continuation of tension up to 28 % strain makes it dominant (Fig. 11c, Fig. 12). As with the 316L steel, it is accompanied by high-preference Cu orientation (4.4 rdm). Thus, with a significant strain generated by tension, the austenite textures of both steel grades are close to each
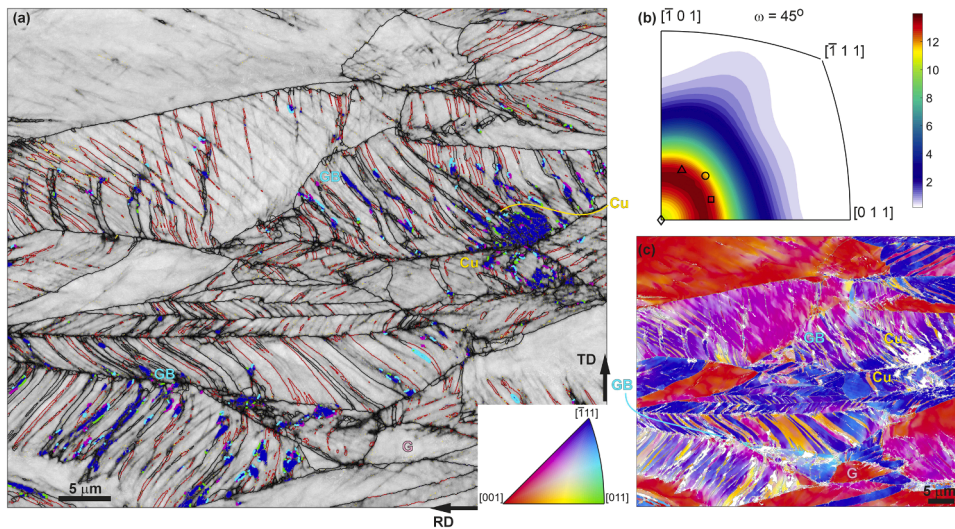
**Fig. 10.** Microstructure of the 316L steel at the fracture. (a) IQ map of austenite together with martensite α' distinguished in blue. Austenite twin boundaries are marked in red, and austenite/α' martensite boundaries with misorientations: Pitsch, KS and NW are denoted in magenta, cyan and green, respectively. (b) MDF for austenite/α'martensite boundaries together with special misorientations: Bain's (rhomb), Pitsch's (square), KS (circle), NW (triangle), (c) austenite in IPF colour coding for TD.
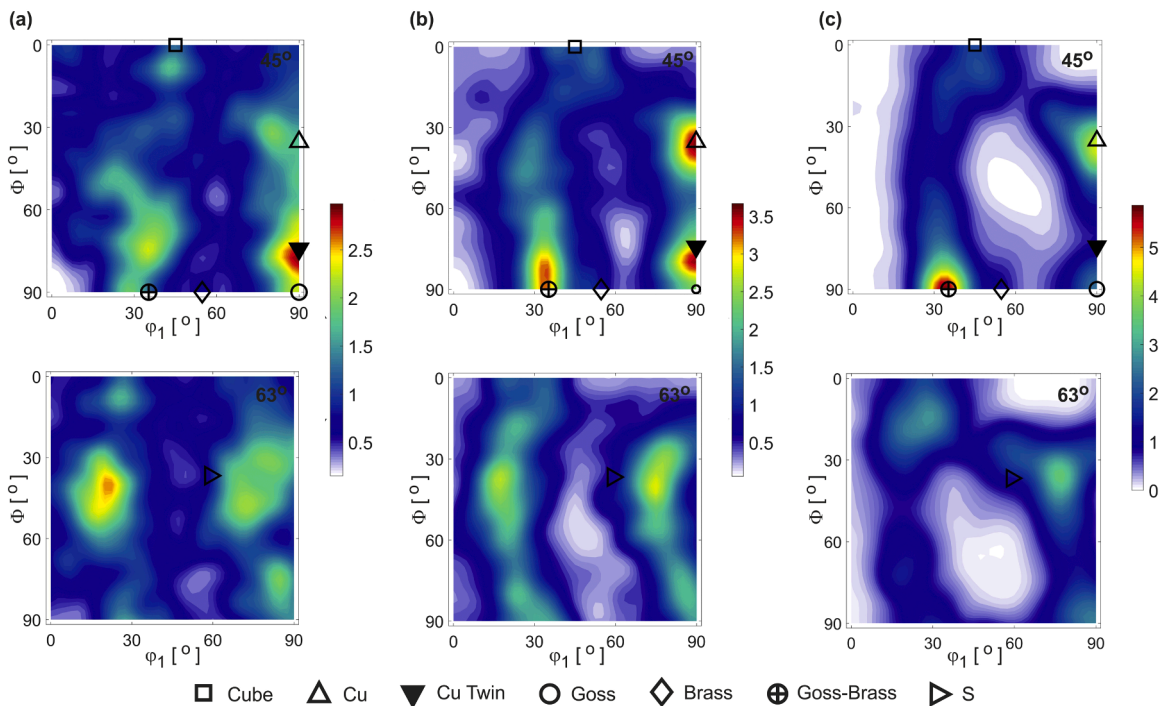


**Fig. 11.** Evolution of the austenitic texture during tension of the 304 steel. Orientation distribution function (ODF) in the Euler space for the sections $\varphi_2 = 45°$ and $\varphi_2 = 63°$ at the strain of 0 (a), 0.11 (b) and 0.28 (c).

other. From this point of view, they are differentiated only by the total volume fraction of Cu and GB orientations. The 304 steel exhibits a stronger Cu and GB preference than the 316L steel.

The in-situ registered microstructure evolution shows the interaction between adjacent austenite grains, which gradually increases the fields with Cu and GB orientations. Areas oriented in such a way tend to shear, which causes the phase transformation to concentrate inside them or on their boundaries. As a result, they gradually transform into martensite α'. The higher content of grains with Cu and GB orientations entails a more significant volume fraction of the secondary phase in 304 than in 316L. The exact
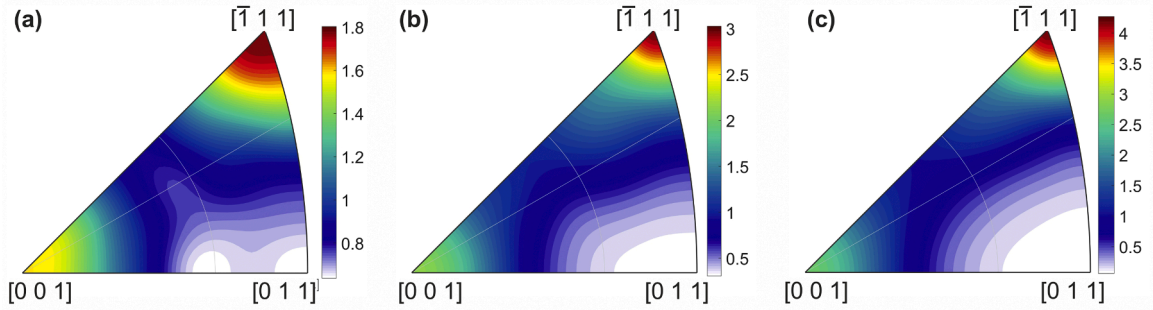
**Fig. 12.** Orientation of austenite grains of the 304 steel with respect to the tension direction at strain 0 (a), 0.11 (b), and 0.28 (c).

observation of the microstructure development reveals that the austenitic areas prone to shearing and martensite α' are distributed evenly, separating the austenite grains which exhibit the ability to undergo significant plastic deformation. Thus, in the 304 steel, unlike 316L, no zones of concentrated strains (macro-slip bands) are formed. The presented mechanism of the microstructural response to axial load explains the mechanical properties determined at the macroscopic level by the DIC method. The key feature of the 304 steel is the uniform distribution of strains in the initial stage of tension with a gradual strain concentration in the area of the front building (Fig. 5b). The observed uniform load transfer is provided by Cu and GB grains, which disperse the grains, generating large deformations due to the activation of the spatially arranged slip systems.

The formation of the matrix orientation system is related to the activity of twins. They tend to align along a common path to start shearing that propagates consecutively across grains. In this way, continual deformation is generated. An example was registered in the in-situ EBSD research (Fig. 13). A twin plate undergoes strain (G1 in Fig. 13), which allows the shear (S1) present in it to continue along the adjacent similarly-oriented twin boundary. The disturbance of the area is identified by the kernel average misorientation (KAM) map (Fig. 13). This process is accompanied by successive shears (S2 and S3) running along paths generated by another twin plate. One of its boundaries initiates an effective shear that connects similarly-oriented twin boundaries (S2). In contrast, the process undertaken by the other (S3) is terminated by the transversely-oriented twin plate. The proceeding shears induce changes in the orientations of a group of grains, which become close to advantageous GB (Fig. 13). A successive effect of the intensive shearing is the phase
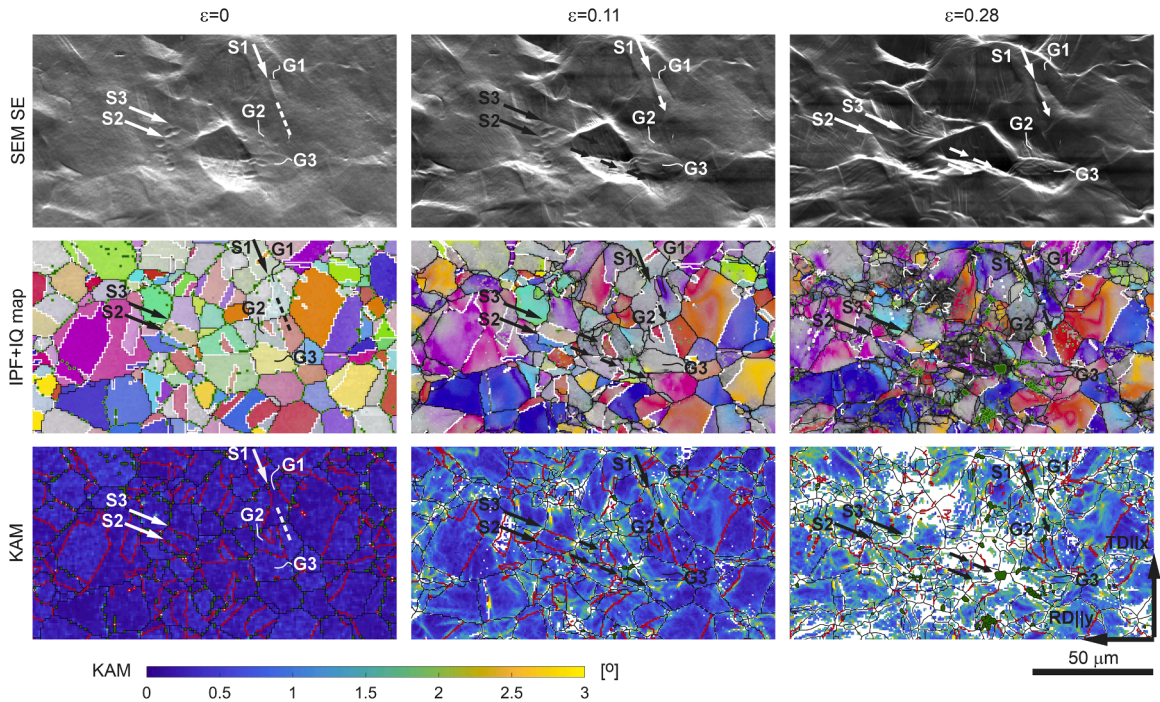


**Fig. 13.** Microstructure evolution of the 304 steel subjected to tension. SEM images, IPF maps for austenite, with respect to the *y* axis, superimposed on IQ maps, and KAM maps for austenite are presented for three strain stages: $\varepsilon = 0$, $\varepsilon = 0.11$, $\varepsilon = 0.28$. Twin boundaries are marked in white (IPF+IQ) or red (KAM), and martensite α' is highlighted in green. The orientation differences between the representative austenite grains and GB for the three presented strain stages are as follows: $G1: 24.5° \rightarrow 21.6° \rightarrow 15.2°$, $G2: 23.5° \rightarrow 25.9° \rightarrow 16.5°$, $G3: 36.3° \rightarrow 28.8° \rightarrow 18.7°$.

transformation. Martensite α' is formed at the intersection of twin boundaries and a twin boundary with a grain boundary (Fig. 13).

Continued tension leads to the necking of the 316L steel specimen, while a visible front is formed in the 304 one. The following question arises: how is such a significant change in the strain (more than 10 %) formed (Fig. 4 d) To explain the propagation of the plastic strain front, the microstructure in the region of the intensive strain gradient was examined (Fig. 14a). The EBSD analysis revealed that, in the front area, there is an increase in the volume fraction of Cu and GB orientations related to the elevated content of martensite α' (Fig. 14b, c). Cu and GB grains, together with martensite α', form a clear matrix in which the austenite grains capable of large plastic deformation are embedded (Figs. 14d and 15b). This spatially organised division of roles resembles the system observed in austenite-martensite dual-phase steel, which exhibits exceptional strength and ductility. Such steel was developed using the ageing process described by Xu et al. (2020). The identified increase in strain results from mass slips leading to the formation of the desired Cu and GB orientations (Fig. 14d). Therefore, Cu and GB grains often form chains (Fig. 15b). The specific arrangement enables the joining of the shear systems of Cu or GB grains, respectively. Along common paths, the intense transformation into martensite α' proceeds (Fig. 15b). It turns out that the GB shear systems $\langle 1\,1\,\overline{2}\rangle\{1\,1\,1\}_\gamma$ are oriented in the same way as active shear systems in the 316L specimen subjected to tension transversely to the rolling direction at 4 K (Nalepka et al., 2024). As a result, the traces left on the surface are inclined at an angle of ±35° with respect to the sample axis (see Fig. 15b), which is characteristic of cryogenic tension. The Cu shear systems $\langle 1\,1\,\overline{2}\rangle\{1\,1\,1\}_\gamma$ with different orientations generate another group of traces. This time, inclined at an angle of ±22° (Fig. 15b). A diametrically different microstructure was registered before the front line (Fig. 15a). The volume content of Cu and GB grains, as well as martensite α', is much lower, while there are often G grains capable of large plastic deformation. The austenite fields are less deformed than those inside the front. The research shows that the front propagation is activated due to the formation of a distinct difference in volume fraction of Cu and GB grains as well as of martensite α' between neighbouring areas. Thus, a gradient microstructure emerging across the front face becomes the source of increased ductility. It turns out that a similar mechanism is responsible for the strength-ductility synergy achieved in the gradient nanostructured 304 steel (Sun et al., 2022). The authors emphasise the pivotal role of dislocation activity in austenite, which is even more significant than the phase transformation.

The 316LN steel is considered as a reference. Microstructure evolution studies reveal a response to tension distinctly different from those found in 304 and 316L (comp. Figs. 16 and 17 to Figs. 7, 8, 11, and 12). The grains with GB orientation contributing to the improvement in mechanical properties initially occur with a high frequency of 3.7 rdm, but their content decreases with tension. When the relative change in the base length reaches 27 %, a neck is formed, and the orientation distribution approaches a random one. The volume content of GB and Cu grains (which strain in a limited way, mainly by shearing) is reduced, while others, prone to significant deformations by the simultaneous activation of several slipping systems, are created: Cube (3.3 rdm), G (2.7 rdm). Such a microstructure cannot further transfer the load applied, and, as a consequence, the specimen fractures.

The increase in random orientations results from strain accumulation frequently combined with the separation of finer grains. Li et al. (2022) also identified such a mechanism in 316LN steel with a mixed-grained structure containing millimetre-grade coarse grains.

To analyse the strain evolution at the microscopic level, KAM values were calculated from the EBSD data collected during the in-situ SEM experiments (see the Supplementary materials for the original IPF and KAM maps). The mechanical response of each studied steel is evaluated based on the arising plastic strain with the elimination of random microstructure disturbances. Thus, it is assumed that the measure of the deformation degree is the fraction of points with KAM values higher than a threshold of 0.6° to all points in the registered representative region. The obtained KAM-based strain functions are presented in Fig. 18. In the initial state, all samples have
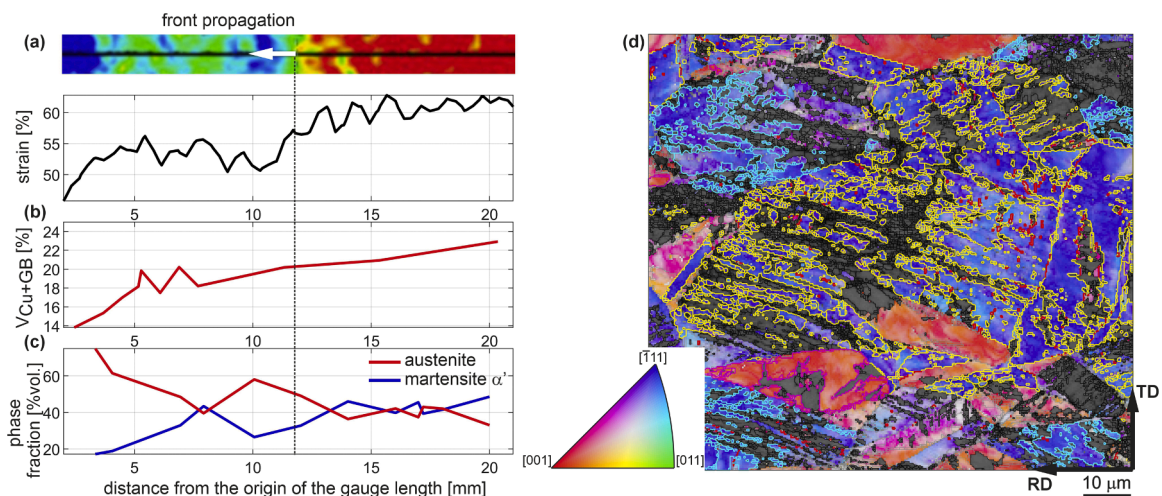


**Fig. 14.** Study of the plastic strain front propagating in the 304 ASS (a) strain distribution according to DIC measurements sets together with the key microstructural changes: volume fraction of Cu and GB orientations (b), volume fraction of phases (c). The strain front is marked by a dashed line. (d) Formation of Cu (yellow boundaries) and GB (cyan boundaries) grains, which subsequently transform by shearing into martensite α' (black areas).
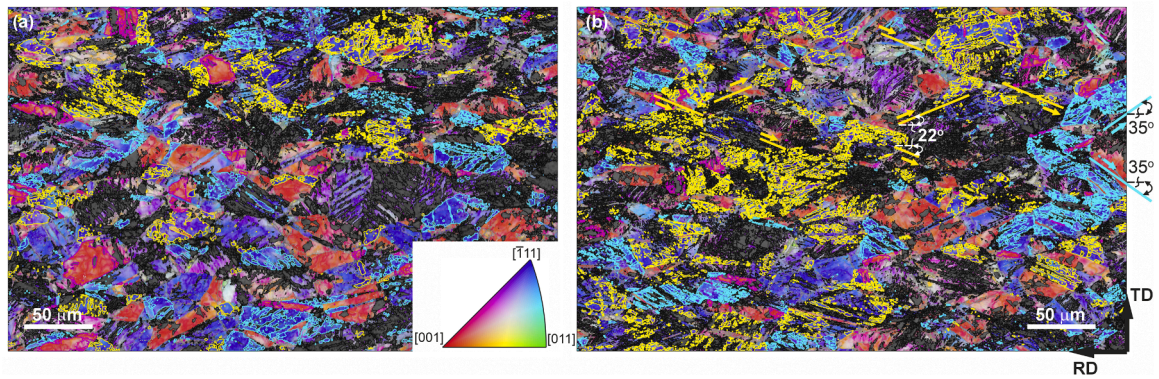
**Fig. 15.** Comparison of the 304 steel microstructure before (a) and inside the strain front (b). Austenite is presented in IPF colour coding and martensite α' is marked in black. Additionally, Cu, GB, and G grains are denoted in yellow, cyan and magenta, respectively. The traces of active shear planes in Cu and GB areas are distinguished in appropriate colours.
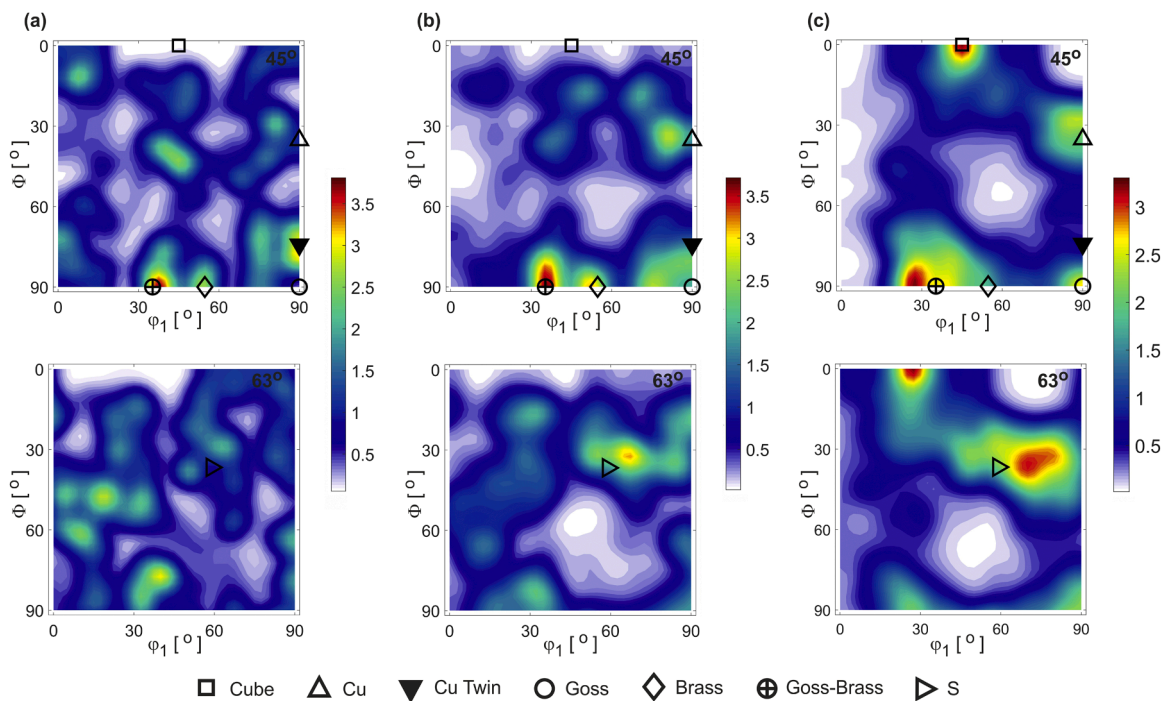


**Fig. 16.** Evolution of the austenitic texture during the tension of the 316LN steel. Orientation distribution function (ODF) in the Euler space for the sections $\varphi_2 = 45°$ and $\varphi_2 = 63°$ at the strain 0 (a), 0.14 (b) and 0.27 (c).

negligible amounts of strained microstructure, from 0.01 to 0.07 of the measurement region. During the first step of the tensile test, the strained areas increase considerably to around 0.5 of the measurement region. Then, some zones arise where the EBSD patterns are not properly indexed due to high strain accumulation. At the next deformation step, when the applied strains reach values between 0.27 and 0.29, depending on the tested steel, the high KAM areas develop further with a significant increase in 316LN and a relatively small change in 304. The 316LN steel reveals the greatest tendency towards strain localisation, which leads to quick necking and failure. Due to the developed surface morphology, the 316LN sample was repolished at this stage, which enabled the registration of the relevant EBSD data. However, to compare 316LN with the other steels, 316L and 304, an EBSD examination of the original, severely-disturbed surface of 316LN was performed and an additional point at the strain of 0.22 was included in the graph. The 316L steel is characterised by a moderate increase in the deformed regions, while 304 reveals the ability to stabilise them thanks to phase transformation leading to strain delocalisation. As a result, the austenite areas that would contribute to higher KAM values are replaced by martensite α'.
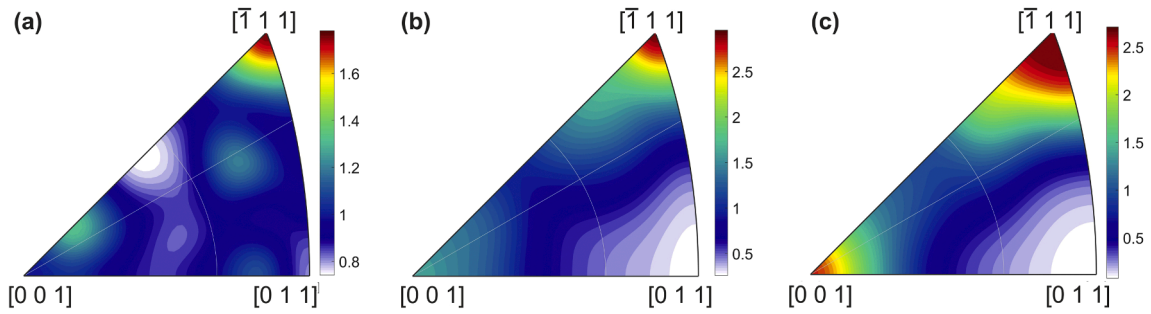
**Fig. 17.** Orientation of austenite grains of the 316LN steel with respect to the tension direction at the strain of 0 (a), 0.14 (b), 0.27 (c).
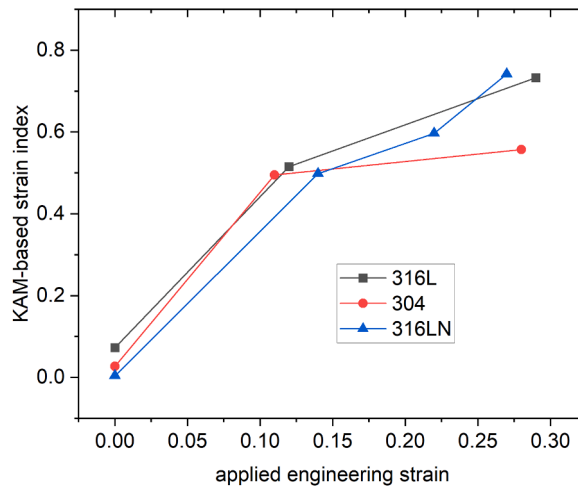


**Fig. 18.** Evolution of the deformation fields in the 304, 316L, and 316LN ASSs identified during the in-situ EBSD tensile tests with the use of the KAM-based strain index.

## 5. Discussion

The results of multiscale identification of plastic behaviour in austenitic stainless steels (304, 316L, 316LN) at room temperature are presented as a basis for the recognition of unstable plastic flow at cryogenic temperatures. Until now, the mechanical and microstructural identification of plastic deformation in austenitic stainless steels was carried out only in a narrow range of temperatures. In this article, the plastic behaviour of ASSs obtained at room temperature is compared to behaviour at cryogenic temperatures (even at 4 K). It turns out that the diffusion-free phase transformation during uniaxial tensile tests of ASSs leads to strain delocalisation and stable propagation of the plastic strain front. For the last effect, the intensity of the phase transformation must be high. Otherwise, the plastic flow instability does not occur in the form of plastic strain front propagation. This is evident from a comparison of the strain distribution during the uniaxial tensile test (Fig. 4) and the intensity of deformation-induced phase transformation of 304 (high-intensity), 316L (low-intensity) and 316LN (absence) at room temperature. For the first time, a new experimental method for its identification is proposed regarding the strain delocalisation effect (Tabin and Brodecki, 2024). It seems that the floating root mean square (RMS) of strain amplitude is able to identify the homogeneity of strain field distribution in 304 and 316L during the uniaxial tensile test (Fig. 5b). A higher RMS value means higher strain heterogeneity in the specimen. The more accurate analysis obtained in this way identifies the key regions requiring further microstructural research. Thus, the RMS of strain amplitude is a tool that efficiently links macroscopic DIC measurements with EBSD investigations. The research at the lower scale reveals that the different modes of the plastic flow and hardening process uncovered by the DIC method for individual grades are closely related to the dissimilar tendency to form Cu and GB orientations (Figs. 7, 11, and 16). The austenite grains of this type undergo limited deformations, mainly through shearing (Fig. 9, Fig. 15). As a result, their mechanical response is similar to that generated by grains of martensite α'. EBSD studies show that twin boundaries are often located within the austenite regions with Cu and GB orientations, regardless of the steel grade. A higher inclination of these grains to the phase transformation is related to the tendency to shear during loading. In fact, extensive martensite α' fields are formed in the Cu and GB regions in both 304 and 316L (Figs. 10 and 15). This observed orientation-based propensity for the phase transformation is confirmed by crystal plasticity simulations performed by Feng et al. (2021). The inverse pole figure (IPF), obtained by these authors for tension, clearly indicates that austenite grains preserving the relationship TD $||\{111\}_\gamma$ exhibit a high preference for strain-induced formation of martensite. The present EBSD studies have captured

a characteristic sequence: austenite grains, by activating several slip systems, adopt the Cu or GB orientations and then undergo an intense phase transformation. A significant concentration of martensite α' occurs at the boundary between the area with limited deformation capacity TD $||\{111\}_\gamma$ (blue according to IPF colour coding) and the region undergoing significant deformation TD$||\{001\}_\gamma$ (red according to IPF colour coding).

The most interesting mechanical behaviour was identified in the 304 steel. The RMS of the strain function registered along the specimen gauge section shows the systematic strain accumulation in one region during the successive stages of the tensile test. When the strain difference between adjacent areas reaches about 10 %, the entire deformation process becomes concentrated in a narrow, propagating zone or a deformation front (Tabin et al., 2023). Interestingly, the propagation of the deformation front is not connected to yield point instability, as observed in some strongly textured magnesium alloys, which seems to be related to dislocation interactions with solute clusters during tension (Pei et al., 2022; Vasilev et al., 2023) or formation of twin bands during cyclic tension-compression tests (Anten & Scholtes, 2019). In this work, the instability in the form of nucleation and propagation of the deformation front occurs in quite late stages of the plastic flow. EBSD studies prove that the source of such behaviour is the difference in the volume fraction of Cu and GB grains and martensite α' as well. Their much higher value, both in the front region and in the area of its previous activity, generates a specimen region with limited deformation capacity, thus showing higher stiffness in relation to the remaining part prone to large deformation realised in the spatial arrangement of slip systems. As a result, two different deformation fields appeared. A tendency to maintain continuity causes an intensive rotation of austenite grains (before the front face) to Cu and GB orientation. In this way, visible chains of such grains are formed, and the mass reorientation realised by slipping generates a stepwise increase in strain. In the next stage, the front is strengthened by the transformation of the Cu and GB areas into martensite α' and then propagates in accordance with the presented mechanism toward the more compliant areas of the specimen.

The 316L steel exhibits different behaviour. From a certain moment, tension at room temperature generates not a single strain concentration zone but several ones with higher strain values. Macroscopically, such a distribution of deformations is confirmed by the RMS function. During tensile tests at room temperature, a neck is formed in one of the strain concentration areas. As a result, the 316L steel is characterised by lower ductility than 304. A difference in mechanical properties came from the microstructural dissimilarity. The grains of the prominent deformation ability are not arranged in a matrix of the Cu and GB grains as in the 304 steel, but they formed bands, with the set being one of the strain concentration zones. This means the ductility is related to the lower orientation preference for Cu and GB. In addition, some distinct areas of the secondary phase are formed intensively in 316L during the last stage of tension, inside the neck. However, the volume content of martensite α' is too small to stabilise the strain increase.

The presented analysis shows that deformation-induced martensite significantly contributes to the specimen response during loading. The observed strain stabilisation is attributed to the non-random embedding of the secondary phase, which forms boundaries with a good lattice matching: NW, KS, and Pitsch. Lowering the temperature to 4 K intensifies the phase transformation, significantly increasing the tensile strength of the 316L steel. A comparison of the presently recorded results with those obtained under cryogenic conditions reveals certain similarities. The mechanical response of the 316L steel at 4 K is close to that observed in the metastable 304 steel at room temperature. Strain is accumulated in a narrow zone, leading to a rapid phase transformation. However, the formed shear band travels differently from that at room temperature. Instead of continuous propagation, the strains arising in a cycle of a serration are located in a narrow interval, which subsequently moves to the adjacent area. One reason for this behaviour is the phase transformation, which intensifies at the boundary of the band and the remaining specimen area. EBSD studies reveal that at room temperature and 4 K, the interaction in the contact zone of two different deformation fields produces martensite. Consequently, the face of a shear band, in which unstable flow in the form of stress drop is realised, is blocked, and the strain localisation is shifted to the neighbouring region of the specimen. The rapid formation of martensite α' results from the separate location of the preferred shear systems that are not joined in continuous paths, as in the case of the 304 steel front propagating at room temperature. As a result, they combine by shearing arbitrarily oriented grains between them, which leads to intensive phase transformation (Nalepka et al., 2024).

The 316LN steel exhibits the lowest ductility and tensile strength. The reasons for this include not only larger grains, which imply lower structural stability, and a lack of phase transformation compared to 304 and 316L but primarily a reduced preference for the Cu and GB components of the developing austenite texture due to tension. The research also reveals that this process contributes to stabilising the increase in strain.

## 6. Conclusions

The experimental results presented in the manuscript can be summarised as follows:

- Deformation-induced phase transformation stabilises the macroscopic shear band propagation in metastable austenitic stainless steels (304, 316L). At room temperature, this strain localisation arises only in the metastable 304 ASS at the final stage of the tensile test. The front, where the strain drop reaches almost 11 %, propagates continuously through the specimen.
- The EBSD studies reveal that, within the shear band arising in the 304 steel at room temperature, a specific austenite texture is formed with a significant presence of Cu and GB components. Grains with these orientations have limited deformation ability, primarily through shearing. Consequently, there is intensive growth of martensite α' in the Cu and GB areas. The microstructure is notably different in the region adjacent to the shear band. There is a reduction in the volume fraction of Cu and GB grains and martensite α', allowing for significant deformations. The resulting gradient leads to the continuous propagation of the shear band. In the front, there is a substantial rotation of grains to Cu and GB orientations, generating strain concentration.
- The shear band is composed of meso-shear bands which consist of joined shear systems of Cu or GB grains forming chains. They enable coherent embedding of martensite α' without stopping the strain front propagation. The uncovered cooperation constitutes

the difference compared to a temperature of 4 K at which the preferred shear systems are formed separately, and their rapid joining induces the phase transformation blocking plastic flow.

- The strain delocalisation can be identified macroscopically by the DIC method. A useful tool is the floating root mean square (RMS) of strain amplitude. A higher RMS value indicates higher strain heterogeneity in the specimen. According to the proposed RMS procedure, the metastable 304 steel exhibits a more uniform strain distribution than 316L during uniaxial tensile tests at room temperature. The reason is a higher content of Cu and GB grains as well as martensite α', which form a matrix trapping areas with high deformation capacity. As the ability to form Cu and GB areas as well as to undergo phase transformation decreases, the mechanism of stabilisation is gradually eliminated. As a result, the 316LN ASS exhibits the lowest ductility.

## CRediT authorship contribution statement

**K. Nalepka:** Writing – original draft, Visualization, Validation, Supervision, Software, Funding acquisition, Formal analysis, Conceptualization. **J. Tabin:** Writing – original draft, Visualization, Validation, Resources, Project administration, Methodology, Investigation, Conceptualization. **J. Kawałko:** Writing – original draft, Visualization, Software, Methodology, Investigation, Data curation. **A. Brodecki:** Investigation, Formal analysis, Data curation. **P. Bała:** Writing – review & editing, Methodology, Funding acquisition. **Z. Kowalewski:** Writing – review & editing, Resources, Funding acquisition.

## Declaration of competing interest

The authors declare that they have no known competing financial interests or personal relationships that could have appeared to influence the work reported in this paper.

## Acknowledgements

## Supplementary materials

Supplementary material associated with this article can be found, in the online version, at doi:10.1016/j.ijplas.2024.104159.

## Data availability

Data will be made available on request.

## References

Angel, T.H., 1954. Formation of martensite in austenitic stainless steels. J. Iron Steel Inst. 177 (5), 165–174.

Anten, K., Scholtes, B., 2019. Formation of macroscopic twin bands and inhomogeneous deformation during cyclic tension-compression loading of the Mg-wrought alloy AZ31. Mater. Sci. Eng.: A 746, 217–228.

Bertinelli, F., Fudanoki, F., Komori, T., Peiro, G., Rossi, L., 2006. Production of austenitic Steel for the LHC superconducting dipole magnets. IEEE Trans. Appl. Superconduct. 16, 1773–1776.

Cios, G., Tokarski, T., Żywczak, A., Dziurka, R., Stępień, M., Gondek, Ł., Marciszko, M., Pawłowski, B., Wieczerzak, K., Bała, P., 2017. The investigation of strain-induced martensite reverse transformation in AISI 304 austenitic stainless steel. Metallurgic. Mater. Trans. A 48, 4999–5008.

Das, A., Chakraborti, P.C., Tarafder, S., Bhadeshia, H.K.D.H., 2011. Analysis of deformation induced martensitic transformation in stainless steels. Mater. Sci. Technol. 27, 366–370.

Devred, A., 2004. Practical low-temperature superconductors for electromagnets, in: CERN Yellow Reports: Monographs, Geneva, CERN.

Feng, Z., Zecevic, M., Knezevic, M., 2021. Stress-assisted (γ→α') and strain-induced (γ→ϵ→α') phase transformation kinetics laws implemented in a crystal plasticity model for predicting strain path sensitive deformation of austenitic steels. Int. J. Plast. 136, 102807.

Fernández-Pisón, P., Rodríguez-Martínez, J.A., García-Tabarés, E., Avilés-Santillana, I., Sgobba, S., 2021. Flow and fracture of austenitic stainless steels at cryogenic temperatures. Eng. Fract. Mech. 258, 108042.

Gao, S., Bai, Y., Zheng, R., Tian, Y., Mao, W., Shibata, A., Tsuji, N., 2019. Mechanism of huge Lüders-type deformation in ultrafine grained austenitic stainless steel. Scr. Mater. 159, 28–32.

Han, W., Liu, Y., Wan, F., Liu, P., Yi, X., Zhan, Q., Morrall, D., Ohnuki, S., 2018. Deformation behavior of austenitic stainless steel at deep cryogenic temperatures. J. Nucl. Mater. 504, 29–32.

Janeiro, I., Hubert, O., Schmitt, J.-H., 2022. In-situ strain induced martensitic transformation measurement and consequences for the modeling of medium Mn stainless steels mechanical behavior. Int. J. Plast. 154, 103248.

Kopec, M., Brodecki, A., Kukla, D., Kowalewski, Z.L., 2021. Suitability of DIC and ESPI optical methods for monitoring fatigue damage development in X10CrMoVNb9-1 power engineering steel. Arch. Civil Mech. Eng. 21, 167.

Levitas, V.I., Chen, H., Xiong, L., 2017. Lattice instability during phase transformations under multiaxial stress: modified transformation work criterion. Phys. Rev. B 96, 054118.

Li, J., Zhou, Z., Wang, S., Mao, Q., Fang, C., Li, Y., Wang, G., Kang, J., Zhu, X., 2020. Deformation mechanisms and enhanced mechanical properties of 304L stainless steel at liquid nitrogen temperature. Mater. Sci. Eng.: A 798, 140133.

Li, Y., Zhang, H., Shang, X., Liu, M., Zhao, S., Cui, Z., 2022. A multiscale investigation on the preferential deformation mechanism of coarse grains in the mixed-grain structure of 316LN steel. Int. J. Plast. 152, 103244.

Meric de Bellefon, G., van Duysen, J.C., Sridharan, K., 2017. Composition-dependence of stacking fault energy in austenitic stainless steels through linear regression with random intercepts. J. Nucl. Mater. 492, 227–230.

Naghizadeh, M., Mirzadeh, H., 2018. Processing of fine grained AISI 304L austenitic stainless steel by cold rolling and high-temperature short-term annealing. Mater. Res. Express. 5, 056529.

Nalepka, K., Skoczeń, B., Ciepielowska, M., Schmidt, R., Tabin, J., Schmidt, E., Zwolińska-Faryj, W., Chulist, R., 2021. Phase transformation in 316L austenitic steel induced by fracture at cryogenic temperatures: experiment and modelling. Materials 14, 127.

Nalepka, K., Skoczeń, B., Schmidt, R., Ciepielowska, M., Schmidt, E., Chulist, R., 2023. Microstructure evolution in the context of fracture in austenitic steels under complex loads at cryogenic temperatures. Mater. Characterisat. 197, 112654.

Nalepka, K., Skoczeń, B., Schmidt, R., Zwolińska-Faryj, W., Schmidt, E., Chulist, R., 2024. Physical mechanism of the intermittent plastic flow at extremely low temperatures. Int. J. Plast. 177, 103994.

Nohara, K., Ono, Y., Ohashi, N., 1977. Composition and grain size dependencies of strain-induced martensitic transformation in metastable austenitic stainless steels. Tetsu-to-Hagane 63, 772–782.

Obst, B., Nyilas, A., 1991. Experimental evidence on the dislocation mechanism of serrated yielding in f.c.c. metals and alloys at low temperatures. Mater. Sci. Eng.: A 137, 141–150.

Olson, G.B., Cohen, M., 1975. Kinetics of strain-induced martensitic nucleation. Metallurgic. Trans. A 6, 791.

Pei, R., Woo, S.K., Yi, S., Al-Samman, T., 2022. Effect of solute clusters on plastic instability in magnesium alloys. Mater. Sci. Eng.: A 835, 142685.

Polatidis, E., Šmíd, M., Hsu, W.N., Kubenova, M., Capek, J., Panzner, T., Van Swygenhoven, H., 2019. The interplay between deformation mechanisms in austenitic 304 steel during uniaxial and equibiaxial loading. Mater. Sci. Eng.: A 764, 138222.

Pustovalov, V.V., 2008. Serrated deformation of metals and alloys at low temperatures (Review). Low Temp. Phys. 34, 683–723.

Rocha, M.R.D., Oliveira, C.A.S.D., 2009. Evaluation of the martensitic transformations in austenitic stainless steels. Mater. Sci. Eng.: A 517, 281–285.

Schmidt, R., Skoczeń, B., Bielski, J., Schmidt, E., 2022. New double surface constitutive model of intermittent plastic flow applied to near 0 K adiabatic shear bands. Mech. Mater. 175, 104500.

Seeger, A., 1957. Dislocations and mechanical properties of crystals, in: Fisher, J.J.C. (Ed.), An International Conference Held at Lake Placid. Wiley, New York.

Skoczeń, B., 2008. Constitutive model of plastic strain induced phenomena at cryogenic temperatures. J. Theor. Appl. Mech. 46, 949–971.

Spencer, K., Véron, M., Yu-Zhang, K., Embury, J.D., 2009. The strain induced martensite transformation in austenitic stainless steels: Part 1 – Influence of temperature and strain history. Mater. Sci. Technol. 25, 7–17.

Sun, Y.T., Kong, X., Wang, Z.B., 2022. Superior mechanical properties and deformation mechanisms of a 304 stainless steel plate with gradient nanostructure. Int. J. Plast. 155, 103336.

Tabin, J., 2021. Kinematic and thermal characteristic of discontinuous plastic flow in metastable austenitic stainless steels. Mech. Mater. 163, 104090.

Tabin, J., Brodecki, A., 2024. Parametrisation of uniform deformation in ductile metals using digital image correlation technology. Exp. Tech. 48, 893–904.

Tabin, J., Nalepka, K., Kawałko, J., Brodecki, A., Bała, P., Kowalewski, Z., 2023. Plastic flow instability in 304 austenitic stainless steels at room temperature. Metallurgic. Mater. Trans. A 54, 4606–4611.

Tabin, J., Skoczen, B., Bielski, J., 2019. Discontinuous plastic flow coupled with strain induced fcc–bcc phase transformation at extremely low temperatures. Mech. Mater. 129, 23–40.

Tabin, J., Skoczen, B., Bielski, J., 2016. Strain localization during discontinuous plastic flow at extremely low temperatures. Int. J. Solids. Struct. 97-98, 593–612.

Vasilev, E., Wang, J., Zhu, G., Knezevic, M., 2023. Influence of deformation banding instabilities on small scale yielding of a Mg–Nd alloy revealed by in-situ digital image correlation. Sci. Rep. 13, 5767.

Wang, Y., Wang, Z., Wang, W., Ma, B., 2023. Effect of nitrogen content on mechanical properties of 316L(N) austenitic stainless steel. Mater. Sci. Eng.: A 884, 145549.

Xu, S.S., Li, J.P., Cui, Y., Zhang, Y., Sun, LX, Li, J., Luan, J.H., Jiao, Z.B., Wang, X.L., Liu, C.T., Zhang, Z.W., 2020. Mechanical properties and deformation mechanisms of a novel austenite-martensite dual phase steel. Int. J. Plast. 128, 102677.

Zhang, X., Yao, Xiao, Yangchuan, Cai, 2024. Effect of Ni element on microstructure and properties of cold-rolled 316L austenitic stainless steel. Mater. Res. Express. 11, 036521.

Zwolińska-Faryj W., Nalepka K., Chulist R., 2022. Phase transformation in austenitic steel AISI 304 induced by complex loads in cryogenic temperatures, 11th European Solid Mechanics Conference, Galway (Ireland).